electronics

Article

Vector Reconfiguration on a Bidirectional Multilevel LCL-T Resonant Converter

Jie Shi, Zhongyi Zhang *, Yi Xu, Dandan Zou and Hui Cao

School of Electrical and Automation Engineering, East China Jiaotong University, Nanchang 330013, China; 8423@ecjtu.edu.cn (J.S.); 20240280808000002@ecjtu.edu.cn (Y.X.); ddzou@ecjtu.edu.cn (D.Z.); 1956@ecjtu.edu.cn (H.C.)

* Correspondence: 3595@ecjtu.edu.cn; Tel.: +86-187-2007-6928

Abstract: With the development of distributed energy technology, the establishment of the energy internet has become a general trend, and relevant research about the core component, energy router, has also become a hotspot. Therefore, the bidirectional isolated DC–DC converter (BIDC) is widely used in AC–DC–AC energy router systems, because it can flexibly support the DC bus voltage ratio and achieve bidirectional power flow. This paper proposes a novel vector reconfiguration on a bidirectional multilevel LCL-T resonant converter in which an NPC (neutral-point clamped) multilevel structure with a flying capacitor is introduced to form a novel active bridge, and a coupling transformer is specially added into the active bridge to achieve multilevel voltage output under hybrid modulation. In addition, an LCL-T two-port vector analysis is adopted to elaborate bidirectional power flow which can generate some reactive power to realize zero-voltage switching (ZVS) on active bridges to improve the efficiency of the converter. Meanwhile, due to the symmetry of the LCL-T structure, the difficulty of the bidirectional operation analysis of the power flow is reduced. Finally, a simulation study is designed with a rated voltage of 200 V on front and rear input sources which has a rated power of 450 W with an operational efficiency of 93.8%. Then, the feasibility of the proposed converter is verified.

Keywords: energy router; bidirectional isolated DC–DC converter; LCL-T; coupling transformer; vector analysis

Citation: Shi, J.; Zhang, Z.; Xu, Y.; Zou, D.; Cao, H. Vector Reconfiguration on a Bidirectional Multilevel LCL-T Resonant Converter. *Electronics* **2024**, *13*, 4557. https://doi.org/10.3390/electronics13224557

Academic Editor: Fabio Corti

Received: 23 September 2024
Revised: 1 November 2024
Accepted: 14 November 2024
Published: 20 November 2024

1. Introduction

1.1. Research Background

In order to achieve the goals of green development and the reasonable distribution of energy resources, reduce pollution emissions, and improve the ecological environment, an investigation into a new generation of renewable and distributed energy interconnection systems is urgent [1–3]. The next-generation new power grid structure represented by the FREEDM system [4,5], proposed by the University of North Carolina in the United States, has played a positive role in the establishment of the China Energy Internet. One of the core parts of the energy internet is the energy router, which has also become a subject hotspot in related research.

1.2. Literature Review

The energy router is normally based on the solid-state transformer (SST) composed of three stages: AC–DC–AC [6–8]. Since the intermediate-stage DC converter needs to take account of the galvanic isolation between the front and rear voltage bus, and can also flexibly provide matching DC bus voltage gain to achieve bidirectional power flow, bidirectional isolated DC–DC converters (BIDCs) [9,10] are generally used. Nevertheless, the dual active bridge (DAB) [11,12] is a typical and representative BIDC structure with many excellent research results, suitable for the working requirements of the BIDC in

various applied situations. However, in the process of power flow, once the voltage gain at the two ends does not match, there will be reactive power loss instead, thereby reducing the efficiency of the converter. A class of control methods represented by DPS [13], EPS [14], TPS [15], and HPS [16] have been proposed one after another to overcome the problem; they are all different combinations of phase shift modulation in bridge and between bridges, to which a PWM duty cycle was added to obtain multiple-degrees-of-freedom control to precisely control the power flow and reduce the generation of reactive power, but with the increase in the degrees of freedom, the control algorithm becomes more and more complicated, and the actual effect is not satisfactory.

In addition, in order for the energy router to be used to medium- and high-power applications, the front-stage rectifier and the back-stage inverter should adopt the NPC multilevel structure [17], which can not only reduce the voltage stress of the switch, but also reduce the THD of the output waveforms. Therefore, the intermediate-stage DC converter should also adopt a multilevel structure for BIDC, which has gradually attracted attention. Based on the traditional two-level DAB converter, some studies [18,19] replace the full-bridge arm with an NPC arm to form a five-level DAB converter, but still adopt the method of DAB mentioned above to manage the converter power bidirectional flow.

Other works [20,21] study the full-bridge LCL-T resonant BIDC, relying on the established relationship of the input, output current, and voltage vector phase for resonant tank two-port networks, so as to analyze the influence law of the active power over the vector phase and PWM duty in the power flow. However, in terms of realizing soft switching, there is less detailed process contact with the modulation method, and analyzing the THD cannot clearly reflect the influence of higher harmonics on power transmission.

1.3. Contribution and Outline

This paper proposes a novel vector reconfiguration on a bidirectional multilevel LCL-T resonant converter. On the basis of the original five-level DAB converter, the traditional series inductor is replaced by an LCL-T tank. A flying capacitor and a coupling transformer are added to the active bridges on both sides to form a multilevel voltage output by hybrid modulation. In addition, reasonable reactive power is generated through the vector phase design, and most active bridge switches on both sides can achieve zero-voltage switching (ZVS) to improve the working efficiency of the BIDC converter. Moreover, due to the symmetry of the LCL-T structure, the bidirectional power flow control characteristics remain consistent, which reduces the difficulty of the quantitative analysis of the converter power flow.

2. The Topology and Multilevel Hybrid Modulation of the Proposed Novel BIDC Converter

2.1. Structure Description of Topology

Figure 1 shows the proposed new multilevel BIDC topology, which is composed of front and rear input sources U_{inp}/U_{ins}, voltage-dividing capacitors C_{1p}~C_{2s}, novel active bridges, and a galvanic isolation module (GIM). Particularly, the two active bridges located on both sides of the GIM have the same structure, and are, respectively, composed of a main bridge arm (MBA) and an auxiliary bridge arm (ABA) that all have an NPC multilevel structure with a flying capacitor and cascaded by coupling transformers TX_p/TX_s with a fixed turns ratio of 1.

In addition, Q_1~Q_4, T_1~T_4 indicate the switches of MBA, Q_5~Q_8, T_5~T_8 indicate the switches of ABA, and D_1~D_8, D_{T1}~D_{T8} are the body diodes to the switches which have the parasitic capacitances C_1~C_8, C_{T1}~C_{T8}. D_{11}~D_{42} are clamping diodes, and C_{f1}~C_{f4} are flying capacitors. Furthermore, the GIM consists of an isolation transformer TX with a turns ratio of k and an LCL-T resonant tank, which includes resonant inductance L_r, resonant capacitor C_r, and leakage inductance L_k.

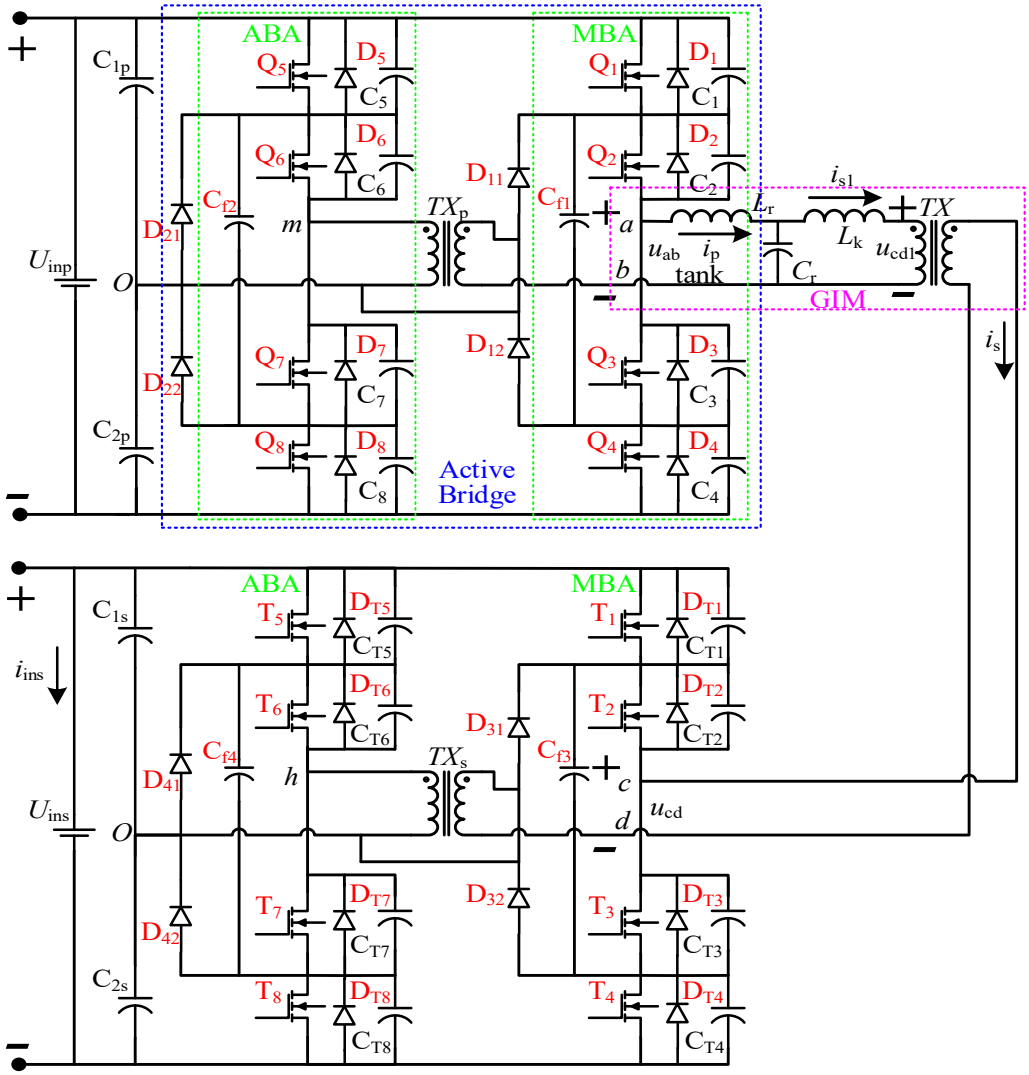

Figure 1. Diagram of topology structure.

2.2. Operation Principles for Multilevel Hybrid Modulation

The active bridge on the left side of the GIM adopts a new multilevel hybrid modulation method by combining phase shift modulation (PSM) with asymmetric pulse width modulation (APWM), in which the PSM angle of the MBA is α, and PSM angle of the ABA is β. Moreover, the MBA's output voltage is u_{ao}, and the ABA's output voltage is u_{mo}, which are both indicated in Figure 1. Thereby, the injecting voltage of GIM is $u_{ab} = u_{ao} + u_{mo}$ by coupling effect of TX_p.

The active bridge on the right side of the GIM also adopts the "PSM + APWM" multilevel hybrid modulation method, in which all switches' sequences only lag behind phase φ to the active bridge on the left side of the GIM. The specific key waveforms of the multilevel hybrid modulation are shown in Figure 2.

The PSM can create a sequence difference among the switches to cause the leading switches Q_1, Q_4 and the lagging switches Q_2, Q_3 in MBA. Particularly, during the dead time, the input current i_p of GIM would charge C_1, C_4 and discharge C_2, C_3 by the path of C_{f1} at the same time to produce a current-exchanging process to realize ZVS of Q_2, Q_3 and obtain zero level, then u_{ao} can output three-level voltage. This stage is cleared in the equivalent circuit of the dead time, as shown in Figure 3.

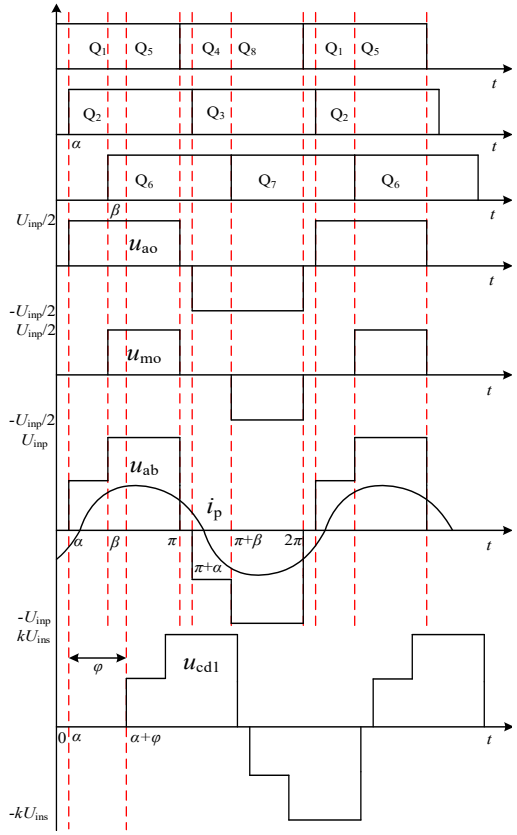

Figure 2. The key waveforms of the multilevel hybrid modulation.

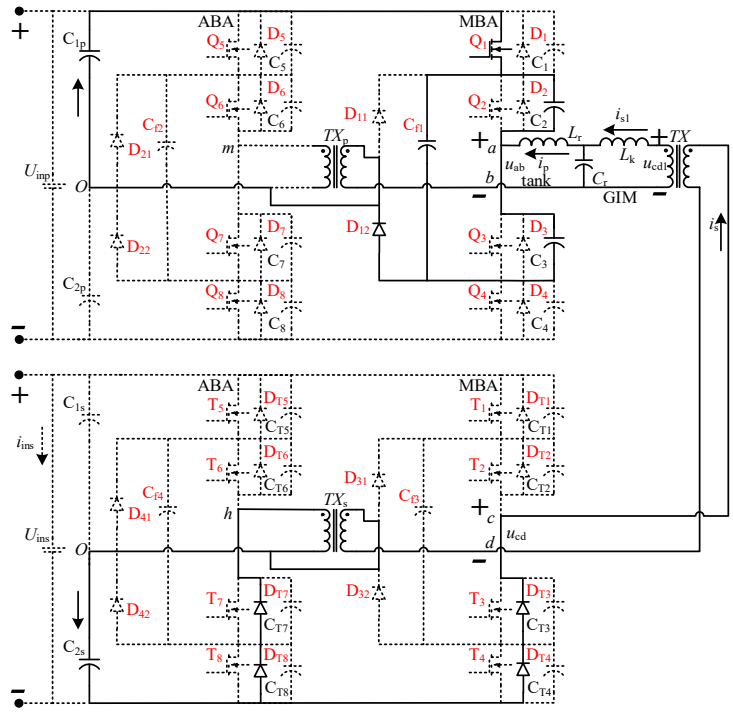

α-t_{DT}~α

Figure 3. The equivalent circuit of the dead time.

Similarly, due to the coupling transformer TX_p, the primary side current of TX_p is clamped by the secondary side current of TX_p, i.e., i_p. Thereby, the leading switches Q_5, Q_8 and lagging switches Q_6, Q_7 in ABA could also have a current-exchanging process between parasitic parameters produced by the primary side current of TX_p to realize ZVS. Nevertheless, when the control of β is different to α, the three-level pulse widths of output voltage are different between u_{mo} and u_{ao}, which makes u_{ab} output five-level voltage after the superposition of u_{mo} and u_{ao}.

3. The Vector Characteristics Analysis of LCL-T Resonant Tank

According to Figure 1, ignoring the magnetizing inductance impedance of the TX, and based on FHA (fundamental harmonic analysis), the equivalent circuit of the two-port network of LCL-T resonant tank can be seen in Figure 4.

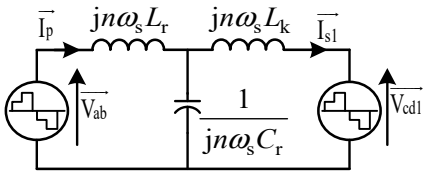

Figure 4. The two-port network of LCL-T resonant tank.

Here, $\dot{I}_p$, $\overrightarrow{V_{ab}}$ are marked as vector of input current i_p, input voltage u_{ab} to the resonant tank; $\overrightarrow{I_{s1}}$, $\overrightarrow{V_{cd1}}$ are marked as vector of output current i_{s1}, out voltage u_{cd1} to the resonant tank; ω_s is the switching angular frequency; n is the harmonic order. Ref. [20] drew the conclusion that voltage vector of Cr would be $\dot{V}_{Cr} = \overrightarrow{V_{ab}} + \overrightarrow{V_{cd1}}$, which means that voltage vector $\overrightarrow{V_{cd1}}$ is equally distributed across L_r and negatively associated with $\dot{I}_p$, and voltage vector $\overrightarrow{V_{ab}}$ is equally distributed across L_k and positively associated with $\overrightarrow{I_{s1}}$; thereby, $\overrightarrow{V_{ab}}$ would be beyond $\overrightarrow{I_{s1}}$ for phase $\pi/2$, and $\dot{I}_p$ would beyond $\overrightarrow{V_{cd1}}$ for phase $\pi/2$. Finally, taking the $\overrightarrow{V_{cd1}}$ as the initial phase reference, the vector phase relationship of each current and voltage on the complex plane is shown in Figure 5.

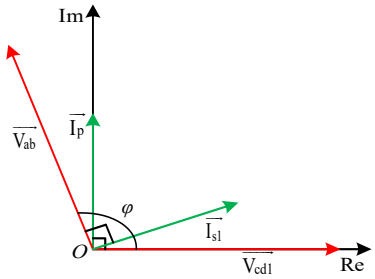

Figure 5. The vector relationship under the ω_r.

Undoubtedly, the current and voltage vector phase relationship on the same side of the two-port network as the resonant tank can be changed by controlling the phase φ between $\overrightarrow{V_{ab}}$ and $\overrightarrow{V_{cd1}}$. When $\varphi = \pi/2$, the $\dot{I}_p$ phase is the same as the $\overrightarrow{V_{ab}}$ phase, and the $\overrightarrow{I_{s1}}$ phase is the same as the $\overrightarrow{V_{cd1}}$ phase. The power is transported from the left active bridge to the right active bridge, which is all active power. When $\varphi > \pi/2$, the $\overrightarrow{V_{ab}}$ phase is beyond the $\dot{I}_p$ phase for φ-$\pi/2$, and the $\overrightarrow{I_{s1}}$ phase is beyond the $\overrightarrow{V_{cd1}}$ phase for φ-$\pi/2$, the direction of power flow remains unchanged, but the transmitted power is contained as part of the reactive power.

When $\varphi = -\pi/2$, the $\overrightarrow{V_{ab}}$ phase lags behind the $\overrightarrow{I_p}$ phase for π, the $\overrightarrow{I_{s1}}$ phase lags behind the $\overrightarrow{V_{cd1}}$ phase for π, and the power is transported from the right active bridge to the left active bridge, which is all reactive power. When $\varphi > -\pi/2$, the $\overrightarrow{V_{ab}}$ phase lags behind the $\overrightarrow{I_p}$ phase for $|\varphi| + \pi/2$, the $\overrightarrow{I_{s1}}$ phase lags behind the $\overrightarrow{V_{cd1}}$ phase for $|\varphi| + \pi/2$, and the direction of power flow remains unchanged, but the transmitted power also is contained as part of reactive power. This paper only analyzes the power flow from the left to the right.

However, according to Figure 2, some reactive power is beneficial to the ZVS of switches. The φ cannot be fixed at $\pi/2$ to eliminate reactive power. In addition, reactive power depends on the phase relation between $\overrightarrow{I_p}$ and $\overrightarrow{V_{ab}}$; thus, the time expression of i_p must be found. Then, the specific vector expressions of $\overrightarrow{V_{ab}}$ and $\overrightarrow{V_{cd1}}$ based on Fourier expansion are derived as follows:

$$\overrightarrow{V_{ab}} = \sum_{n=1,3,5\cdots}^{\infty} \overrightarrow{V_{ab}(n)} = \sum_{n=1,3,5\cdots}^{\infty} \frac{U_{inp}}{\sqrt{2}n\pi}[\cos(n\beta) + 3 - j\sin(n\beta)] \tag{1}$$

$$\overrightarrow{V_{cd1}} = \sum_{n=1,3,5\cdots}^{\infty} \overrightarrow{V_{cd1}(n)} = \sum_{n=1,3,5\cdots}^{\infty} \frac{kU_{ins}}{\sqrt{2}n\pi} \begin{bmatrix} \cos(n\beta+\varphi) + 3\cos(\varphi) - \\ j(\sin(n\beta+\varphi) + 3\sin(\varphi)) \end{bmatrix} \tag{2}$$

Because the transmission characteristics of the two-port network are only related to the internal structure, the admittance matrix can be established as (3), on the basis of Figure 4:

$$Y = \begin{bmatrix} Y_{11} & Y_{12} \\ Y_{21} & Y_{22} \end{bmatrix} \tag{3}$$

where

$$\begin{cases} Y_{11} = \frac{1-(n\omega_s)^2 L_k C_r}{j\left(n\omega_s L_r + n\omega_s L_k - (n\omega_s)^3 L_r C_r L_k\right)} \\ Y_{12} = Y_{21} = \frac{-1}{j\left(n\omega_s L_r + n\omega_s L_k - (n\omega_s)^3 L_r C_r L_k\right)} \\ Y_{22} = \frac{1-(n\omega_s)^2 L_r C_r}{j\left(n\omega_s L_r + n\omega_s L_k - (n\omega_s)^3 L_r C_r L_k\right)} \end{cases} \tag{4}$$

Then,

$$\overrightarrow{I_p(n)} = \frac{\left(1-(n\omega_s)^2 L_k C_r\right)\overrightarrow{V_{ab}(n)} - \overrightarrow{V_{cd1}(n)}}{j\left(n\omega_s L_r + n\omega_s L_k - (n\omega_s)^3 L_r C_r L_k\right)} \tag{5}$$

$$\overrightarrow{I_{s1}(n)} = \frac{\left(1-(n\omega_s)^2 L_r C_r\right)\overrightarrow{V_{cd1}(n)} - \overrightarrow{V_{ab}(n)}}{j\left(n\omega_s L_r + n\omega_s L_k - (n\omega_s)^3 L_r C_r L_k\right)} \tag{6}$$

where $\overrightarrow{I_p(n)}$, $\overrightarrow{I_{s1}(n)}$, $\overrightarrow{V_{ab}(n)}$, and $\overrightarrow{V_{cd1}(n)}$ indicate nth harmonic vectors. Then, based on Equations (1), (2), (5), and (6), the input active power to the resonant tank can be derived as follows:

$$\begin{aligned} P_{in} &= \sum_{n=1,3,5\cdots}^{\infty} p_{in}(n) = \sum_{n=1,3,5\cdots}^{\infty} \mathrm{Re}\left[\overrightarrow{V_{ab}(n)} \cdot \overrightarrow{I_p^*(n)}\right] = f(U_{inp}, U_{ins}, k, L_r, L_k, C_r, \omega_s, \beta, \varphi, n) \\ &\sum_{n=1,3,5\cdots}^{\infty} \left[\begin{array}{l} \frac{U_{inp}(\cos(n\beta)+3)\cdot\left[kU_{ins}(\sin(n\beta+\varphi)+3\sin(\varphi)) - \sqrt{2}n\pi\left(1-(n\omega_s)^2 L_k C_r\right)\sin(n\beta)\right]}{2(n\pi)^2\left(n\omega_s L_r + n\omega_s L_k - (n\omega_s)^3 L_r C_r L_k\right)} + \\ \frac{U_{inp}\sin(n\beta)\cdot\left[kU_{ins}(\cos(n\beta+\varphi)+3\cos(\varphi)) - U_{inp}\left(1-(n\omega_s)^2 L_k C_r\right)(\cos(n\beta)+3)\right]}{2(n\pi)^2\left(n\omega_s L_r + n\omega_s L_k - (n\omega_s)^3 L_r C_r L_k\right)} \end{array} \right] \end{aligned} \tag{7}$$

The input reactive power to the resonant tank can also be derived as follows:

$$Q_{\text{in}} = \sum_{n=1,3,5\cdots}^{\infty} q_{\text{in}}(n) = \sum_{n=1,3,5\cdots}^{\infty} \text{Im}\left[\overrightarrow{\text{V}_{\text{ab}}(n)} \cdot \overrightarrow{\text{I}_{\text{p}}^{*}(n)}\right] = f(U_{\text{inp}}, U_{\text{ins}}, k, L_{\text{r}}, L_{\text{k}}, C_{\text{r}}, \omega_{\text{s}}, \beta, \varphi, n)$$
$$\sum_{n=1,3,5\cdots}^{\infty}\left[\begin{array}{l} -\dfrac{U_{\text{inp}}(\cos(n\beta)+3)\cdot\left[kU_{\text{ins}}(\cos(n\beta+\varphi)+3\cos(\varphi))-U_{\text{inp}}\left(1-(n\omega_{\text{s}})^2L_{\text{k}}C_{\text{r}}\right)(\cos(n\beta)+3)\right]}{2(n\pi)^2\left(n\omega_{\text{s}}L_{\text{r}}+n\omega_{\text{s}}L_{\text{k}}-(n\omega_{\text{s}})^3L_{\text{r}}C_{\text{r}}L_{\text{k}}\right)}- \\ \dfrac{U_{\text{inp}}\sin(n\beta)\cdot\left[kU_{\text{ins}}(\sin(n\beta+\varphi)+3\sin(\varphi))-\sqrt{2}n\pi\left(1-(n\omega_{\text{s}})^2L_{\text{k}}C_{\text{r}}\right)\sin(n\beta)\right]}{2(n\pi)^2\left(n\omega_{\text{s}}L_{\text{r}}+n\omega_{\text{s}}L_{\text{k}}-(n\omega_{\text{s}})^3L_{\text{r}}C_{\text{r}}L_{\text{k}}\right)} \end{array}\right] \quad (8)$$

According to Equations (7) and (8), the transmission characteristics of P_{in} and Q_{in} depend on up to 10 related parameters, making it too difficult to obviously show the clear influence law of each variable. Thus, we let ω_s equal resonant angular frequency $\omega_{\text{r}} = 1/\sqrt{L_{\text{r}}C_{\text{r}}}$, which can make the vector relationship mentioned before, on the basis of Figure 5, be more precise, because almost all power flow depends on the transmission of the fundamental wave when the input impedance of the resonant tank is increasing, as ω_s is close to ω_r. And the time expression of i_p for analysis can be replaced by fundamental component i_{p_1} which is derived as shown in (9) according to (5) under $k = 1$, $U_{\text{inp}} = U_{\text{ins}}$, $L_r = L_k$:

$$i_{\text{p\_1}}(t) = \frac{\sqrt{2}U_{\text{inp}}}{\pi}\sqrt{\frac{C_{\text{r}}(3\cos(\beta)+5)}{L_{\text{r}}}}\cdot\sin\left(\frac{t}{\sqrt{L_{\text{r}}C_{\text{r}}}}+\arctan\left(\frac{\cos(\beta+\varphi)+3\cos(\varphi)}{\sin(\beta+\varphi)+3\sin(\varphi)}\right)\right) \quad (9)$$

Furthermore, the Q_{in}/P_{in} ratios of total power flow can be completely expressed by $q_{in}(1)/p_{in}(1)$, i.e., Q_1/P_1 ratios. Thereby, the variation law of the Q_1/P_1 with β and φ is established, as shown in Figure 6.

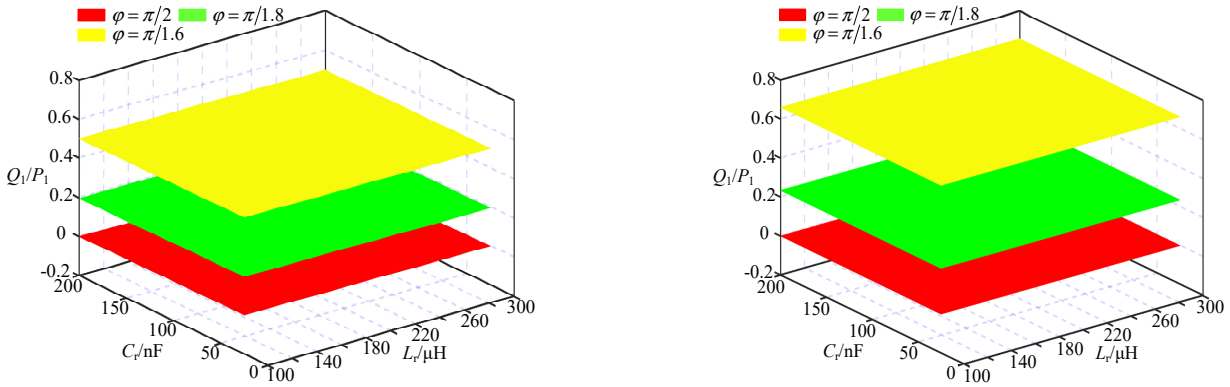

(**a**) $\beta = \pi/5$ (**b**) $\beta = 2\pi/5$

Figure 6. The variation law of the Q_1/P_1 with β and φ.

It is obvious that the Q_1/P_1 ratios both extremely increase with the growth of φ when $\beta = \pi/5$ and $\beta = 2\pi/5$, as shown in Figure 6a,b, and the Q_1/P_1 ratios of $\varphi = \pi/1.8$, $\varphi = \pi/1.6$ in Figure 6b are both larger than the Q_1/P_1 ratios of $\varphi = \pi/1.8$, $\varphi = \pi/1.6$ in Figure 6a, which means that the parameters of β and φ both have positive correlation with the Q_1/P_1 ratios, but this correlation of β will be enhanced with the growth of φ. Particularly, the structure parameters L_r and C_r of the resonant tank have no effect on the variation law of the Q_1/P_1 with β and φ; this means that the inherent variation characteristics of Q_1/P_1 only depend on the proposed novel BIDC topology and hybrid modulation. But there must be a trade-off to ensure that the Q_1/P_1 ratio remains within a reasonable range to realize ZVS, and these two aspects are both dependent on the design of the related parameters β and φ.

4. The Design of ZVS to Active Bridge Switches Located on Both Sides of GIM

Having established the topology and multilevel hybrid modulation of the proposed novel BIDC converter in Section 3, it is essential to examine the design of ZVS for the active bridge switches situated on either side of the GIM. This transition is necessary as the efficient operation of the converter is contingent upon the successful implementation of ZVS, which in turn is contingent upon the topological structure and modulation strategy outlined in the previous section.

4.1. The Relationship Between Turn-Off Current and ZVS

According to (7), the initial phase of i_{p_1} is indicated as θ_{p_1}:

$$\theta_{p\_1} = \arctan\left(\frac{\cos(\beta+\varphi)+3\cos(\varphi)}{\sin(\beta+\varphi)+3\sin(\varphi)}\right) \tag{10}$$

When $\theta_{p\_1} < 0$, the $\overrightarrow{I_p}$ phase lags behind the $\overrightarrow{V_{ab}}$ phase to generate some reactive power. The variation of the θ_{p_1} with respect to $\beta \in [0, \pi]$ and $\varphi \in [\pi/2, \pi/1.6]$ is illustrated in Figure 7 using (10).

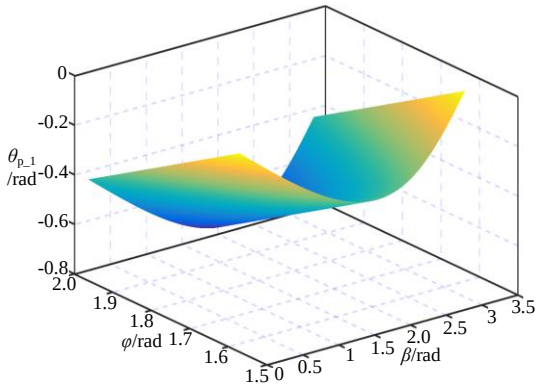

Figure 7. The variations law of the θ_{p_1} with β and φ.

The initial phase θ_{Q1} of sequences to the Q_1, Q_5 are both zero on the basis of Figure 2. It can be found that θ_{p_1} lags behind θ_{Q1}, according to Figure 7, and the magnitude of the turn-off current $i_{p\_1\_off}$ on the turn-off moment of $t = \pi\sqrt{L_r C_r}$ to the Q_1, Q_5 is derived as $|i_{p\_1}(0)| = i_{p\_1}(\pi\sqrt{L_r C_r}) = i_{p\_1\_off}$ due to the cyclic symmetry property of the i_{p_1}.

Thus, the variation law of the $i_{p\_1\_off}$ with β and φ is also shown in Figure 8, which shows that $i_{p\_1\_off}$ will increase with the growth of each of β, φ, C_r, and decrease with the growth of L_r, but it would be $i_{p\_1\_off} > 0$ regardless of the values of these parameters. This means that $i_{p\_1\_off}$ will not change the previous polarity to produce a current-exchanging process to realize ZVS after Q_1, Q_5 are both turned off.

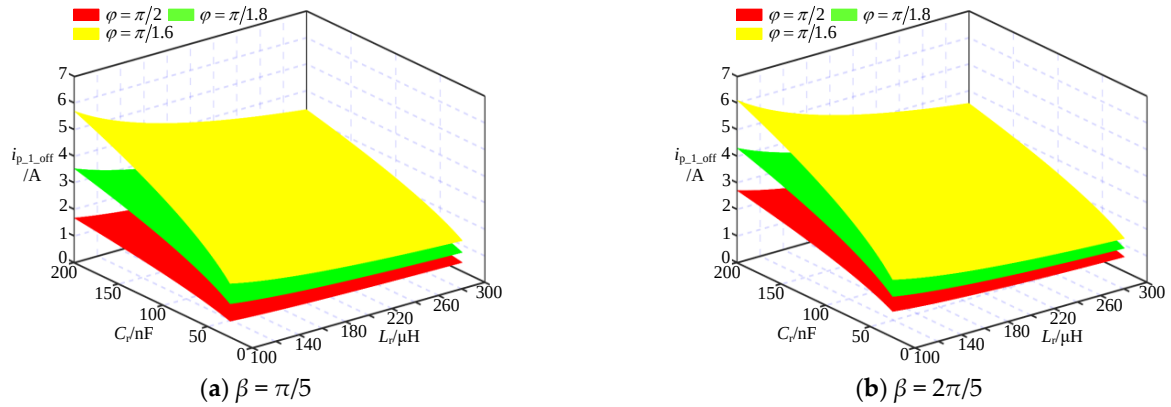

(**a**) $\beta = \pi/5$ (**b**) $\beta = 2\pi/5$

Figure 8. The variation law of the $i_{p\_1\_off}$ with β and φ.

Furthermore, in view of the current-exchanging process for realizing ZVS, which has to provide enough power, the charge conservation law between $i_{p\_1\_off}$ and stored energy of the parasitic capacitances should be established as follows (11):

$$i_{p\_1\_off} \cdot t_{\mathrm{DT}} = 4 \cdot C_{\mathrm{oss}} \cdot \frac{U_{\mathrm{inp}}}{2} \tag{11}$$

where $i_{p\_1\_off}$ would be treated as a constant in the dead time t_{DT} due to the very short time; the quantities of parasitic capacitances for all switches are uniformly indicated as C_{oss}; and 4 represents the number of switches involved in the ZVS process for MBA or ABA. Then, the range of magnitude of the turn-off current is

$$i_{p\_1\_off} \geq 4 \cdot C_{\mathrm{oss}} \cdot \frac{U_{\mathrm{inp}}}{2t_{\mathrm{DT}}} \tag{12}$$

4.2. The Achievement of ZVS for Lagging Switches of MBA, ABA by Designing PSM Angles α, β

The initial phase θ_{Q2} of sequences to Q_2 is closer to θ_{p_1} than Q_1, Q_5, making the magnitude of the turn-off current smaller, which might cause the failure of ZVS, as shown in Figure 2, because the LCL-T resonant tank has only one resonance angular frequency, ω_r, without the circulating current stage, compared with the LLC resonant tank under PSM. Thereby, a relationship of $\alpha \leq |\theta_{p\_1}|$ must be guaranteed to realize ZVS. Based on Figure 7, the contour cross-curves map of θ_{p_1} is shown in Figure 9, where the contour cross-curves are indicated as solid-colored lines under each specific value of θ_{p_1}. Moreover, referring to (9), (10), the magnitude range of the turn-off current $i_{p\_1\_off\_L}$ on the turn-off moment of $t = (\pi + \alpha)\sqrt{L_{\mathrm{r}}C_{\mathrm{r}}}$ to the Q_2 for realizing ZVS is derived as follows (13):

$$i_{p\_1\_off\_L} = i_{\mathrm{p\_1}}\left((\pi + \alpha)\sqrt{L_{\mathrm{r}}C_{\mathrm{r}}}\right) = \left|i_{\mathrm{p\_1}}(\alpha\sqrt{L_{\mathrm{r}}C_{\mathrm{r}}})\right| \geq 2 \cdot C_{\mathrm{oss}} \cdot \frac{U_{\mathrm{inp}}}{2t_{\mathrm{DT}}} \tag{13}$$

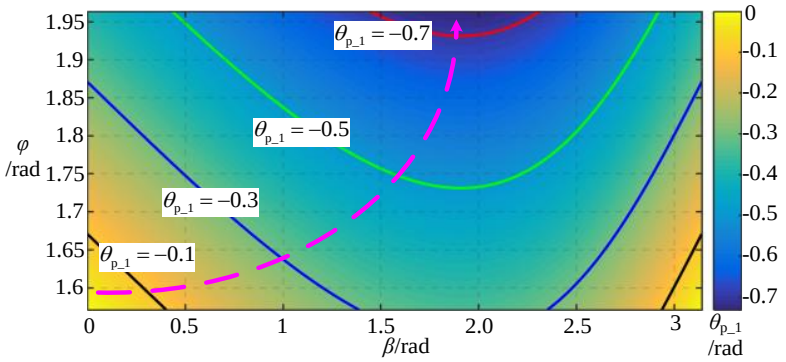

Figure 9. The contour cross-curves map of θ_{p_1}.

Along the dotted arrow direction, $|\theta_{p\_1}|$ will be increased with the increase in β, φ, and then the adjustable α is also increased. However, φ should not be taken as a larger value, in order to limit the ratio of reactive power to keep the efficiency of the converter, and β should be larger, to make $\alpha \leq |\theta_{p\_1}|$. In addition, β must also satisfy $\beta \leq |\theta_{p\_1}|$ to realize ZVS of Q_6 in ABA, as was also analyzed for α, because of the coupling effect of TX_p.

However, β *is* usually larger than α and $|\theta_{p\_1}|$, mainly to control the power flow under the limitation of φ. In addition, u_{ab} can output five-level voltage only once Q_1, Q_5 realize ZVS to output the three-level voltage of MBA or ABA clamped by PSM.

4.3. The Design of ZVS for the Right Side Active Bridge Switches

i_{s1} can also be replaced by the fundamental component i_{s1_1}. According to Figure 5, the $\overrightarrow{I_{s1}}$ phase lags behind the $\overrightarrow{I_p}$ phase for π-φ, and we have π-$\varphi < \varphi$ to make the initial phase θ_{s1_1} of i_{s1_1}, derived as follows (14):

$$\theta_{s1\_1} = \arctan\left(\frac{\cos(\beta+\varphi)+3\cos(\varphi)}{\sin(\beta+\varphi)+3\sin(\varphi)}\right) - (\pi-\varphi) = -\arctan\left(\frac{\sin(\beta)}{\cos(\beta)+3}\right) - \frac{\pi}{2} \quad (14)$$

i_{s1_1} can be derived as shown in (15), according to (6) combined with (14):

$$i_{s1\_1}(t) = \frac{\sqrt{2}U_{ins}}{\pi}\sqrt{\frac{C_r(3\cos(\beta)+5)}{L_k}} \cdot \sin\left(\frac{t}{\sqrt{L_kC_r}} - \arctan\left(\frac{\sin(\beta)}{\cos(\beta)+3}\right) - \frac{\pi}{2}\right) \quad (15)$$

It can be plotted as a function image of $f(\beta,\varphi) = \theta_{s1\_1} + \varphi$ with zero boundary, as shown in Figure 10, to analyze the relationship between θ_{s1_1} and the initial phase $\theta_{T1,}$ which is equal to $-\varphi$ and aligns at the leading switches T_1, T_5.

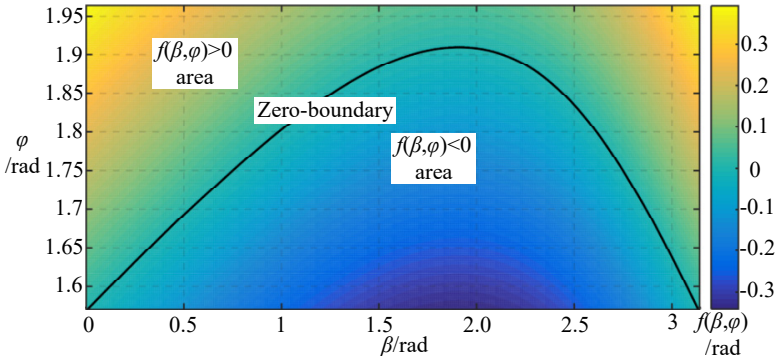

Figure 10. The function image of $f(\beta, \varphi) = \theta_{s1\_1} + \varphi$.

When in the $f(\beta,\varphi)$ area, θ_{s1_1} will exceed θ_{T1} to provide the turn-off current $i_{s1\_1\_off}$ on the turn-off moment of $t = (\pi+\varphi)\sqrt{L_kC_r}$ to the T_1, T_5. However, i_{s1_1} is inputted on the right side active bridge, compared with $i_{p\_1,}$ which is outputted on the left side active bridge. Thus, $i_{s1\_1\_off}$ will also not change the previous polarity to produce the current-exchanging process to realize ZVS after T_1, T_5 are both turned off. In addition, it can be found that β has to be taken as a small value under the limitation of φ to keep $f(\beta,\varphi) > 0$. Then, the modulation key waveforms of the right side active bridge can be plotted in Figure 11 on the basis of Figure 2:

In the same way, the charge conservation law between $i_{s1\_1\_off}$ and the stored energy of the parasitic capacitances C_{oss} should be enough to complete ZVS, which is still applied to Equations (11) and (12). And it can also obviously be seen that the ZVS of lagging switches T_2, T_6 is easier to realize than T_1, T_5, according to Figure 11. It must be emphasized that the transient analysis of another half working period to the converter will be skipped for brevity due to the mechanism similar to the abovementioned one. In addition, in subsequent simulations based on the SABER platform, the simulation results for the other half of the converter's working period will also be skipped for brevity due to the simulation symmetry.

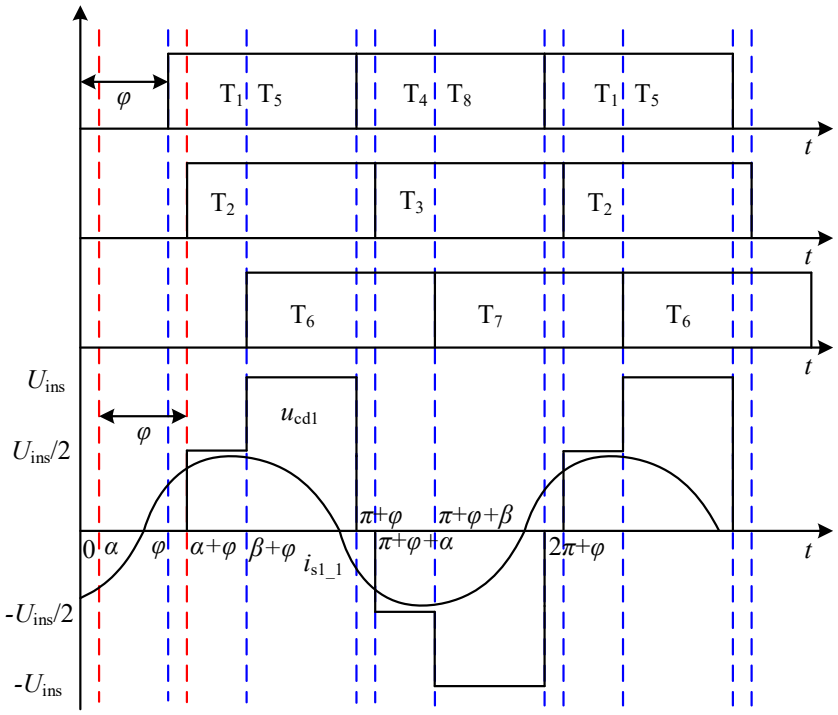

Figure 11. The modulation key waveforms of the right side active bridge.

5. The Simulation Design of Prototype

5.1. Simulation Parameters Design

The simulation study is based on the SABER platform, and the relevant parameters are shown in Table 1.

Table 1. The parameters of the 450 W Simulink experiment.

Components	Values
U_{inp}/U_{ins}	200 V
ω_s	$2\pi \times 50 \times 10^3$ rad/s
C_{1p}~C_{2s}	940 μF
C_r	50 nF
L_r/L_k	200 μH
TX_p/TX_s	1:1
TX	1:1
Q_1~Q_8, T_1~T_8	IRF460 MOSFETs
D_{11}~D_{42}	Power diode
C_{f1}~C_{f4}	1 μF
Control Variables	**Values**
φ	$\pi/1.8$ (5.5 μs)
α	$2\pi/25$ (0.8 μs)
β	$\pi/5$ (2 μs)
t_{DT}	0.5 μs

5.2. The Checking Calculation of Parameters

The C_{oss} of the MASK model to IRF460 MOSFETs is set to 480 pF, and the parameters of Table 1 are substituted into (9). Then, the inequality relation of (12) can be satisfied by calculation:

$$i_{p\_1\_off} = 1.248 \geq 4 \cdot C_{oss} \cdot \frac{U_{inp}}{2t_{DT}} = \frac{4 \cdot 480\text{pF} \cdot 200\text{V}}{2 \cdot 0.5\mu\text{s}} = 0.384 \quad (16)$$

Moreover, inequality relations of $\alpha \leq |\theta_{p\_1}|$ and (13) can be satisfied by calculation:

$$\alpha = \frac{2\pi}{25} \leq \left|\arctan\left(\frac{\cos(\beta+\varphi)+3\cos(\varphi)}{\sin(\beta+\varphi)+3\sin(\varphi)}\right)\right| = 0.328$$
$$i_{p\_1\_off\_L} = 0.296 \geq 2 \cdot C_{oss} \cdot \frac{U_{inp}}{2t_{DT}} = 0.192 \quad (17)$$

In practice, when β is significantly bigger than $|\theta_{p\_1}|$, the proposed converter may fail to achieve ZVS of lagging switches Q_2, Q_6 in ABA to the left side active bridge.

The parameters of Table 1 are also substituted into (14), yielding $f(\beta, \varphi) = 0.0214 > 0$, indicating that the conditions for ZVS have been met. And $\left|i_{s1\_1\_off}\right| = \left|i_{s1\_1}\left((\pi+\varphi)\sqrt{L_k C_r}\right)\right|$ = 0.083 A, calculated by (15), is not in agreement with (12), which shows that there is not enough power for the charge conservation law to complete ZVS. Thus, maybe only the leading switches T_1, T_4 and T_5, T_8 in MBA and ABA will fail to provide ZVS to the right side active bridge.

5.3. The Key Waveforms of Simulation Study

The simulation output results were processed to form the simulation study key waveforms shown in Figure 12, which are the same as Figures 2 and 11, with the transient detail of t_{DT}.

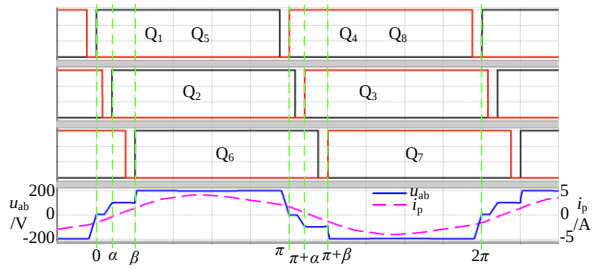

(**a**) simulation waveforms to left side active bridge

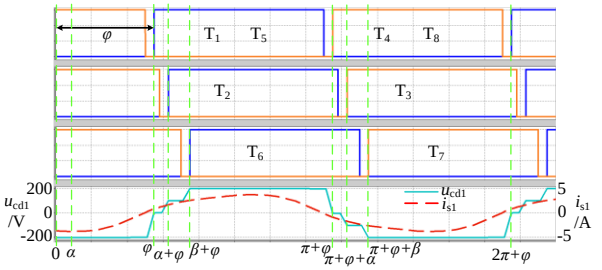

(**b**) simulation waveforms to right side active bridge

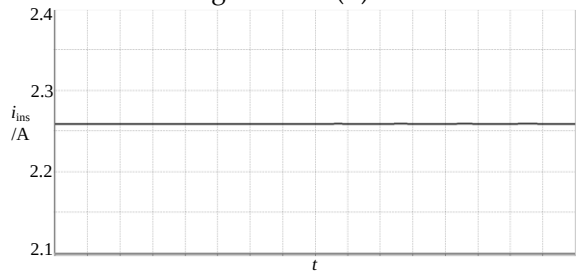

(**c**) output current i_{ins}

Figure 12. The simulation study key waveforms.

In Figure 12a, firstly, i_p is bigger than zero in t_{DT} after turning off Q_1, Q_5. u_{ab} falls from 200 V to 0 at the same time, which shows that the ZVS of the leading switches in MBA and ABA have been realized. Secondly, u_{ab} falls from 0 to −100 V in t_{DT}, which shows that the ZVS of the lagging switches in MBA have been realized, while i_p is still bigger than zero after turning off of Q_2. Thirdly, u_{ab} falls from −100 V to −200 V after turning on Q_7, not after turning off Q_6, which shows that the ZVS of the lagging switches in ABA have not been realized, because i_p is less than zero in t_{DT}. The simulation results are consistent with the design of Section 5.2.

In Figure 12b, i_{s1} is less than zero in t_{DT} after turning off T_1, T_5. u_{cd1} falls from 200 V to 0 at the same time, which shows that the ZVS of the leading switches in MBA and ABA have been realized, which is different from the design of Section 5.2, because higher-order harmonics also transmit power. In addition, the ZVS of lagging switches in MBA and ABA is easier to realize after turning off T_2 and T_6, respectively, while u_{cd1} falls from 0 V to −100 V and falls from −100 V to −200 V, respectively, as shown in the simulation study

key waveforms, which are consistent with the expectation of Section 4.3. In Figure 12c, the active power absorbed by the right side active bridge is approximately equal to 450 W due to the output current $i_{\mathrm{ins}} \approx 2.25$ A. Particularly, according to (1) and (5), and under $k = 1$, $U_{\mathrm{inp}} = U_{\mathrm{ins}}$, $L_r = L_k$, the active power generated by the left side active bridge can be derived as follows:

$$P_{\mathrm{in}} = \sum_{n=1,3,5\cdots}^{\infty} p_{\mathrm{in}}(n) = \sum_{n=1,3,5\cdots}^{\infty} \mathrm{Re}\left[\overrightarrow{\mathrm{V_{ab}}(n)} \cdot \overrightarrow{\mathrm{I_p^*}(n)}\right] = f'(U_{\mathrm{inp}}, L_{\mathrm{r}}, C_{\mathrm{r}}, \beta, \varphi, n) \quad (18)$$

Then, $P_{\mathrm{in}}(1)$ can be calculated to equal 422 W by substituting the parameters of Table 1 into Equation (18), which shows an operational efficiency of 93.8% and the feasibility of the proposed converter.

5.4. The Performance Evaluation of the Proposed Converter

The proposed novel active bridge is formed by two NPC (neutral point clamped) multilevel structures with flying capacitors, which, respectively, act as the main bridge arm (MBA) and auxiliary bridge arm (ABA). As we know, the NPC multilevel structure can reduce the voltage stresses of switches to half of the input voltage of the converter, which keeps costs down, when the ZVS of switches is implemented. And, for example, generally, in the emerging 800 V charging system of an EV battery, the proposed converter can select the rated 650 V of MOSFETs to meet the 400 V of requirement for maximum voltage stress within safety margins, while the conventional full bridge LCL-T resonant converter [22] has to select the rated 1200 V of MOSFETs to meet the 800 V of requirement for maximum voltage stress within safety margins. Sometimes, the higher the voltage level, the more expensive it is. The product menus of Digi-Key Co. LTD, Thief River Falls, MN, USA, contain the Rohm Semiconductor SCT3120 ALGC11 (SiC) (650 V 21 A USD 10.45) the and Rohm Semiconductor SCT3105 KRC14 (SiC) (1200 V 24 A USD 24.86). Furthermore, the switching frequency adopted in the proposed converter is higher than the conventional DAB converter [23], reducing the volume of magnetic components and enabling a higher power density, which is also used for keeping costs down. However, due to the vector reconfiguration, more phase shift angles are introduced into the modulation in the active bridge, which makes ZVS implementation and the design and transfer control of active or reactive power more complex.

6. Conclusions

A novel active bridge for multilevel output, leveraging an NPC multilevel structure and a coupling transformer, operates under "PSM + APWM" modulation. By integrating this bridge with LCL-T resonance, a bidirectional multilevel converter is proposed, enabling bidirectional power flow and ZVS for most switches through reactive power design based on vector analysis with flexible phase shift controls α, β, and φ. The simulation on the SABER platform confirms the feasibility of the 450 W bidirectional converter.

Author Contributions: Conceptualization, H.C.; methodology, Y.X.; formal analysis, Z.Z.; investigation, J.S. and D.Z.; writing—original draft preparation, Z.Z.; writing—review and editing, Y.X.; project administration, Z.Z.; funding acquisition, J.S. and H.C. All authors have read and agreed to the published version of the manuscript.

Funding: This research was funded by Youth Fund Project of Department of Education of Jiangxi Province of China, grant number GJJ2200659; Youth Fund Project of Department of Transportation of Jiangxi Province of China, grant number 2024QN012; and Natural Science Foundation of Jiangxi Province of China, grant number 20232ACB204024.

Data Availability Statement: The original contributions presented in this study are included in the article. Further inquiries can be directed to the corresponding author(s).

Conflicts of Interest: The authors declare no conflicts of interest.

References

1. Hussain, S.M.S.; Nadeem, F.; Aftab, M.A.; Ali, I.; Ustun, T.S. The Emerging Energy Internet: Architecture, Benefits, Challenges, and Future Prospects. *Electronics* **2019**, *8*, 1037. [CrossRef]
2. Kabalci, Y.; Kabalci, E.; Padmanaban, S.; Holm-Nielsen, J.B.; Blaabjerg, F. Internet of Things Applications as Energy Internet in Smart Grids and Smart Environments. *Electronics* **2019**, *8*, 972. [CrossRef]
3. Wang, K.; Yu, J.; Yu, Y.; Qian, Y.; Zeng, D.; Guo, S.; Xiang, Y.; Wu, J. A Survey on Energy Internet: Architecture, Approach, and Emerging Technologies. *IEEE Syst. J.* **2018**, *12*, 2403–2416. [CrossRef]
4. Huang, A.Q.; Crow, M.L.; Heydt, G.T.; Zheng, J.P.; Dale, S.J. The Future Renewable Electric Energy Delivery and Management (FREEDM) System: The Energy Internet. *Proc. IEEE* **2011**, *99*, 133–148. [CrossRef]
5. She, X.; Lukic, S.; Huang, A.Q.; Bhattacharya, S.; Baran, M. Performance Evaluation of Solid State Transformer Based Microgrid in FREEDM Systems. In Proceedings of the IEEE Applied Power Electronics Conference and Exposition (APEC), Fort Worth, TX, USA, 6–11 March 2011. [CrossRef]
6. Liu, X.; Liu, L.; Li, H.; Corzine, K.; Guo, T. Study on the Start-Up Schemes for the Three-Stage Solid State Transformer Applications. In Proceedings of the 2012 IEEE Energy Conversion Congress and Exposition (ECCE), Raleigh, NC, USA, 15–20 September 2012. [CrossRef]
7. Yao, T.; Leonard, I.; Ayyanar, R.; Steurer, M. Single-Phase Three-Stage SST Modeling Using RTDS for Controller Hardware-in-the-Loop Application. In Proceedings of the 2015 IEEE Energy Conversion Congress and Exposition (ECCE), Montreal, QC, Canada, 20–24 September 2015. [CrossRef]
8. Zhou, J.; Wang, J. Research Review on Multi-Port Energy Routers Adapted to Renewable Energy Access. *Electronics* **2024**, *13*, 1493. [CrossRef]
9. Pellitteri, F.; Miceli, R.; Schettino, G.; Viola, F.; Schirone, L. Design and Realization of a Bidirectional Full Bridge Converter with Improved Modulation Strategies. *Electronics* **2020**, *9*, 724. [CrossRef]
10. She, X.; Huang, A.Q.; Burgos, R. Review of Solid-State Transformer Technologies and Their Application in Power Distribution Systems. *IEEE J. Emerg. Sel. Top. Power Electron.* **2013**, *1*, 186–198. [CrossRef]
11. De Doncker, R.; Divan, D.; Kheraluwala, M. A Three-Phase Soft-Switched High-Power-Density DC/DC Converter for High-Power Applications. *IEEE Trans. Ind. Appl.* **1991**, *27*, 63–73. [CrossRef]
12. Kheraluwala, M.; Gascoigne, R.; Divan, D.; Baumann, E. Performance Characterization of a High-Power Dual Active Bridge DC-to-DC Converter. *IEEE Trans. Ind. Appl.* **1992**, *28*, 1294–1301. [CrossRef]
13. Bai, H.; Mi, C. Eliminate Reactive Power and Increase System Efficiency of Isolated Bidirectional Dual-Active-Bridge DC–DC Converters Using Novel Dual-Phase-Shift Control. *IEEE Trans. Power Electron.* **2008**, *23*, 2905–2914. [CrossRef]
14. Zhao, B.; Yu, Q.; Sun, W. Extended-Phase-Shift Control of Isolated Bidirectional DC–DC Converter for Power Distribution in Microgrid. *IEEE Trans. Power Electron.* **2012**, *27*, 4667–4680. [CrossRef]
15. Wu, K.; de Silva, C.W.; Dunford, W.G. Stability Analysis of Isolated Bidirectional Dual Active Full-Bridge DC–DC Converter with Triple Phase-Shift Control. *IEEE Trans. Power Electron.* **2012**, *27*, 2007–2017. [CrossRef]
16. Shen, Y.; Sun, X.; Li, W.; Wu, X.; Wang, B. A Modified Dual Active Bridge Converter with Hybrid Phase-Shift Control for Wide Input Voltage Range. *IEEE Trans. Power Electron.* **2016**, *31*, 6884–6900. [CrossRef]
17. Ma, Z.; Niu, H.; Zhang, X.; Wu, X.; Cai, X. Virtual Space Vector Overmodulation Strategy for NPC Three-Level Inverters with Common-Mode Voltage Suppression. *IEEE Trans. Power Electron.* **2024**, *39*, 6877–6888. [CrossRef]
18. Song, C.; Sangwongwanich, A.; Yang, Y.; Pan, Y.; Blaabjerg, F. Analysis and Optimal Modulation for 2/3-Level DAB Converters to Minimize Current Stress with Five-Level Control. *IEEE Trans. Power Electron.* **2023**, *38*, 4596–4612. [CrossRef]
19. Liu, P.; Chen, C.; Duan, S. An Optimized Modulation Strategy for the Three-Level DAB Converter with Five Control Degrees of Freedom. *IEEE Trans. Ind. Electron.* **2020**, *67*, 254–264. [CrossRef]
20. Twiname, R.P.; Thrimawithana, D.J.; Madawala, U.K.; Baguley, C.A. A New Resonant Bidirectional DC–DC Converter Topology. *IEEE Trans. Power Electron.* **2014**, *29*, 4733–4740. [CrossRef]
21. Saha, T.; Bagchi, A.C.; Wang, H.; Zane, R.A. Bidirectional LCL-T Resonant DC–DC Converter for Priority Loads in Undersea Distribution Networks. *IEEE Trans. Power Electron.* **2022**, *37*, 14874–14887. [CrossRef]
22. Guo, Z.; Li, M. An Optimized DPS Control Strategy for LCL Resonant Dual Active Bridge Converter for Wide Voltage Conversion Ratio. *IEEE J. Emerg. Sel. Top. Ind. Electron.* **2021**, *2*, 501–512. [CrossRef]
23. Liu, B.; Davari, P.; Blaabjerg, F. Nonlinear C_{oss}-V_{DS} Profile Based ZVS Range Calculation for Dual Active Bridge Converters. *IEEE Trans. Power Electron.* **2021**, *36*, 45–50. [CrossRef]